SAND2015-10808C

Resonance Characteristics of Transonic Flow over a Rectangular Cavity using Pulse-Burst PIV

Steven J. Beresh,[1] Justin L. Wagner,[2] Edward P. DeMauro,[3] John F. Henfling,[4] Russell W. Spillers[5]
Sandia National Laboratories, Albuquerque, NM, 87185

Pulse-burst particle image velocimetry (PIV) has been used to acquire time-resolved data at 37.5 kHz of the flow over a finite-width rectangular cavity at Mach 0.6, 0.8, and 0.94. Power spectra of the PIV data reveal four resonance modes that match the frequencies detected simultaneously using high-frequency wall pressure sensors. Velocity resonances exhibit spatial dependence in which the lowest frequency acoustic mode is active within the recirculation region whereas the three higher modes are concentrated within the shear layer. Spatio-temporal cross-correlations were calculated from velocity data first bandpass filtered for specific resonance frequencies. The low-frequency acoustic mode shows properties of a standing wave without spatial correlation. Higher resonance modes are associated with alternating coherent structures whose size and spacing decrease for higher resonance modes and increase as structures convect downstream. The convection velocity appears identical for all resonance modes, but it too increases with downstream distance. This is in contrast to the well-known Rossiter equation, which assumes a convection velocity constant in space.

Introduction

In recent years, time-resolved particle image velocimetry (TR-PIV) has evolved as a means of measuring temporally correlated velocity fields, allowing the acquisition of PIV movies to add a time component to fluid dynamics investigations. Whereas TR-PIV has emerged in a variety of low-speed flows as an adaptation of PIV technology using diode-pumped solid-state kHz-rate lasers and fast CMOS cameras, the requirements of high-speed flows exceed the capabilities of these technologies. Instead, TR-PIV in high-speed flows is best accomplished using a pulse-burst laser, as this is the only light source capable of producing sufficient energy at the necessarily rapid pulse rates, though with the penalty of a very low duty cycle. Simultaneous with the maturation of pulse-burst laser technology, quality high-speed cameras have begun to achieve desirable framing rates without excessive sacrifice of the size of the spatial array. Pulse-burst PIV has a minimal history. Wernet appears to have been the first to achieve pulse-burst PIV [1], with more recent development offered by Brock et al [2] and Miller et al [3, 4]. Pulse-burst PIV had not seen application in a wind tunnel or other testing facility until Beresh et al demonstrated its use in a transonic wind tunnel [5].

The time-resolved capability of pulse-burst PIV can play a key role in the understanding of the physics of resonances in high-speed cavity flows. TR-PIV measurements of cavity resonance have been achieved previously in water tunnels [6-8] and in a 4-m/s wind tunnel [9, 10], but never at the high velocities relevant to aircraft aerodynamics. This distinction is significant because incompressible cavity flows may induce self-sustained oscillations but not resonance and therefore do not reproduce the conditions found once the speed of sound instills significant delays. TR-PIV data can reveal the growth of shear layer vortices and their recirculation within the

---

[1] Distinguished Member of the Technical Staff, Engineering Sciences Center, AIAA Associate Fellow, correspondence to: P.O. Box 5800, Mailstop 0825, (505) 844-4618, email: sjberes@sandia.gov

[2] Senior Member of the Technical Staff, AIAA Senior Member

[3] Post-Doctoral Appointee, AIAA Member

[4] Distinguished Technologist, AIAA Senior Member

[5] Principal Technologist

This work is supported by Sandia National Laboratories and the United States Department of Energy. Sandia is a multiprogram laboratory managed and operated by Sandia Corporation, a wholly owned subsidiary of Lockheed Martin Corporation, for the United States Department of Energy's National Nuclear Security Administration under contract DE-AC04-94AL85000.

cavity, the large-scale motion of the recirculation region, and ejection events at the aft end of the cavity. The behavior of these flowfield structures is key to the acoustic tones produced by the cavity resonance and in compressible cavity flows it can be well explored using the temporally correlated velocity fields of pulse-burst PIV.

It is well known that flow over a cavity produces resonant tones that can reach very high pressure levels, which are popularly known as Rossiter modes [11] and whose frequencies are reasonably predicted for rectangular cavities by Heller and Bliss's equation [12]. These acoustic modes are most readily identified by using high-frequency pressure sensors, but they have been identified in the velocity field using laser Doppler velocimetry [13-15] and can be observed in the aforementioned low-speed TR-PIV experiments [9, 10]. But the Rossiter equation and Heller and Bliss's version of it are dependent upon empirical constants that nominally represent the aeroacoustic properties within the cavity but in reality have been tuned for optimal agreement with observed resonances.

The dominant turbulent structures present in the flowfield should correspond to the resonance observed in the unsteady wall pressures and this relationship has been explored by previous studies. Murray and Ukeiley [16, 17] and Zhang and Naguib [18] conditioned velocity fields on simultaneous pressure measurements to identify differences in the flowfield structure as a function of the resonance mode and phase, and Haigermoser [6] used instantaneous drag as a condition. Kegerise et al [19] accomplished something similar using schlieren imaging. The streamwise spacing of the dominant turbulent structures has been shown to reasonably correspond to the wavelength expected based on the cavity resonance frequency [10, 16, 19, 20]. These studies provide important insight linking the velocity field to the acoustic resonances, but much remains to be understood regarding how cavity flowfield features induce specific resonance tones.

The present experiment implements pulse-burst PIV in a finite-width rectangular cavity at Mach numbers of 0.6, 0.8, and 0.94. Previous studies by the present authors [21, 22] have used conventional PIV to establish the mean flowfield structure and its turbulence intensity distribution as a function of the width of the cavity and the Mach number. A more recent effort has begun to correlate the flowfield dynamics from the conventional PIV velocity fields with simultaneous high-frequency pressure measurements [23] and a companion paper to the present document examines this relationship using the same pulse-burst PIV data set [24]. In this work, the temporal component of the velocity field is used to determine the spatial distributions of cavity resonance modes and to identify the characteristics of flowfield structures associated with the different resonance modes.

Experimental Apparatus

Experiments were conducted in Sandia's Trisonic Wind Tunnel (TWT). The TWT is a blowdown-to-atmosphere facility using air as the test gas, whose test section is enclosed within a pressurized plenum. In its transonic configuration, the test section is a straightforward rectangular duct of dimensions 305 × 305 mm^2 (12 × 12 inch^2) with interchangeable walls for porous or solid boundaries. Porous walls ordinarily are used for testing near sonic conditions when blockage relief is needed and solid walls are used when imaging diagnostics require windows. In the present case, transonic experiments were conducted at Mach numbers 0.60, 0.80, and 0.94 and conditions were selected to hold the freestream dynamic pressure q_∞ constant to a nominal value of about 33 kPa with a fixed stagnation temperature of 321K ± 2K. Freestream velocities U_∞ were measured from previous PIV experiments as 215, 280, 315 m/s for the three Mach numbers, respectively. Previous PIV measurements and Pitot probe surveys have shown that the incoming 99%-velocity boundary layer thickness varies from about 10 – 15 mm for the Mach range of the present experiments, which is 40-60% of the cavity depth (see below).

The cavity is simply a rectangular pocket installed into the lower wall of the test section, having dimensions 127 × 127 mm^2 (5 × 5 inch^2) with a nominal depth of 25.4 mm (1 inch), as in [21, 22]. The test section was configured with porous walls on the top wall and one side wall to alleviate non-physical resonances due to wind tunnel duct modes [25]; a solid wall with a window for imaging was installed in the other side of the test section. A glass floor allowed the laser sheet to enter the cavity from below. The streamwise (x), wall-normal (y), and spanwise (z) coordinate system originated at the spanwise center of the cavity leading edge with y pointed away from the cavity.

The TWT is seeded by a thermal smoke generator (Corona Vi-Count 5000) that produces a large quantity of particles typically 0.2 - 0.3 μm in diameter from a mineral oil base. Particles are delivered to the TWT's stagnation chamber upstream of the flow conditioning section through a series of pipes and tubes, in which agglomeration of the particles occurs. Previous measurement of the *in-situ* particle response across a shock wave generated by a wedge shows the particle size to be 0.7 - 0.8 μm. Stokes numbers have been estimated as at most 0.05 based on *a posteriori* analysis of PIV measurements, which is sufficiently small to rapidly attain the local velocity and reduce particle lag errors to a negligible level.

In the current work, a quasi-continuous burst-mode laser (QuasiModo-1000, Spectral Energies, LLC) with both diode- and flashlamp-pumped Nd:YAG amplifiers was used to produce a high-energy pulse train at 532 nm. The pulse-burst laser generates a burst of maximum duration 10.2 ms once every 8 seconds with a maximum repetition rate of 500 kHz. It produces 532-nm pulse energy of 500 mJ at its lowest repetition rate of 5 kHz and 20 mJ pulse energy at its highest repetition rate. The laser is capable of producing doublets with variable interpulse spacing at all repetition rates, though in the present work the time between pulses in a doublet was 3.40 μs ± 1 ns for Mach 0.8 and was adjusted to 4.5 and 3.0 μs for Mach 0.6 and 0.94, respectively. In this work, 37.5 kHz doublets were used for PIV measurements with energy per pulse of 27 mJ for 10.2 ms burst duration. The design of the pulse-burst laser is based on master oscillator power amplifier architecture and is similar to previously reported pulse-burst-mode lasers [26-28].

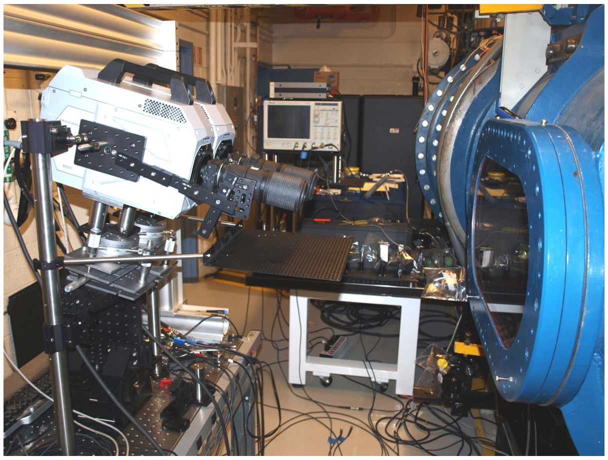

Fig. 1: Two high-speed cameras aligned side-by-side for imaging an extended field of view and peering downwards into the cavity.

The pulse-burst PIV images were acquired using two high-speed CMOS cameras (Photron SA-Z) which have a full framing rate of 20 kHz and an array of 1024 × 1024 pixels at this speed. The camera windowing function allows the framing rate to be increased by sampling a semi-arbitrary portion of the imaging array. In the present case, each camera operated at 75 kHz with an array of 640 × 360 pixels. The two pulses in a doublet were frame-straddled around the cameras' interframe transfer time, which allowed cross-correlation analysis of pairs of images; thus PIV velocity fields were acquired at nominally 37.5 kHz (actually, 37.495 kHz). In all cases, the cameras were equipped with 200-mm focal length lenses.

The two cameras were placed side by side to extend the field of view in the streamwise direction, yielding a combined field of view of approximately 103 × 31 mm^2 for two-component PIV. Unfortunately, the large size of the camera bodies precluded placing them sufficiently close to one another to image the laser sheet from a normal direction. Therefore, they were canted at an angle of 3.5 deg such that their individual imaging regions were adjacent and could be combined for vector processing. This angle creates a perspective bias on the velocity vectors due to added sensitivity to the out-of-plane velocity component, but calculations estimate that the maximum induced error is no more than 2%. In addition, the cameras were angled downward by 12 deg to view about 55% into the depth of the cavity. This introduced a larger bias error in the vertical velocity component, estimated to reach as much as 20%; however, past experience has shown that this does not hinder visualization of the cavity flow or detection of turbulent eddies [29]. Scheimpflug mounts maintained focus despite the inclined view. A photo of the SA-Z cameras installed adjacent to the wind tunnel is shown in Fig. 1; their downward inclination is evident.

Approximately 250 bursts of velocity fields have been obtained at each of the three Mach numbers. This provides for an examination of Mach number effects within the transonic regime and much improved statistical convergence in comparison to the initial data set described in [5]. Data were processed using LaVision's DaVis v8.2. Image pairs were background-corrected, intensity normalized, and then interrogated with an initial pass using 64 × 64 pixel interrogation windows, followed by two iterations of 24 × 24 pixel interrogation windows. A 50% overlap in the interrogation windows was used as well. The spatial resolution of each vector is approximately 1 × 1 mm^2. The resulting vector fields were validated based upon signal-to-noise ratio, nearest-neighbor comparisons, and allowable velocity range.

Results and Discussion

Velocity Fields

A mean field of the streamwise velocity component with superposed streamlines is shown in Fig. 2 at Mach 0.8, acquired using a conventional stereoscopic PIV system as part of the experimental campaign described in [22]. These data were acquired prior to the pulse-burst PIV and were illuminated by a typical 10-Hz dual-cavity Nd:YAG laser rather than the pulse-burst laser and images were captured using low-speed PIV cameras (LaVision sCMOS). The shear layer is conspicuous due to the vertical gradient of the streamwise velocity and grows markedly before its impingement on the aft cavity wall. The recirculation region is evident in both the strong recirculation velocities and the extent of the streamlines, and it can be seen to dominate the cavity flowfield and stretch over nearly its entire streamwise length. The figure is representative of the mean flowfield at Mach 0.6 and 0.94 as well. The mean

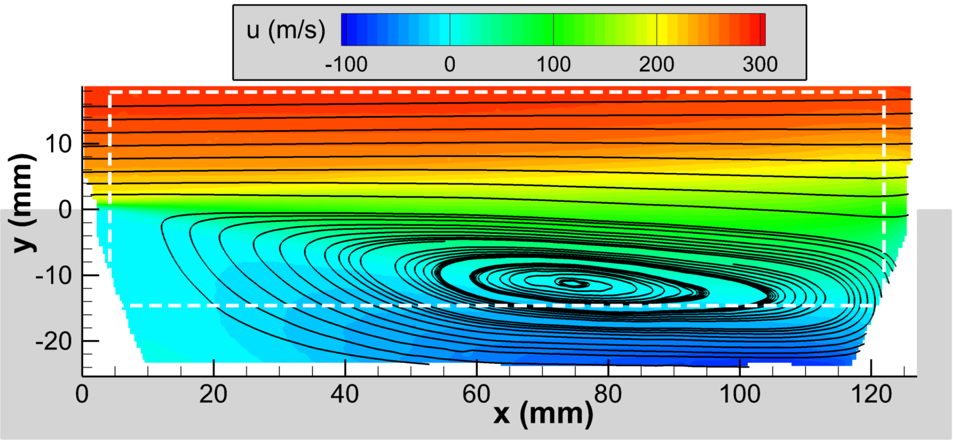

Fig. 2: Mean streamwise velocity field at Mach 0.8 with superposed streamlines, which is representative of the general flow structure for all cases. Obtained using conventional stereoscopic PIV. The white box shows the field of view of the pulse-burst PIV measurements in subsequent figures.

features of the cavity strongly resemble those measured in other cavities of similar length-to-depth ratio despite their acquisition in a two-dimensional configuration rather than the present finite-width geometry [6, 30-32], and it is consistent with the narrow incompressible cavity of [33]. The white box drawn in Fig. 2 shows the more limited field of view of the pulse-burst PIV in subsequent figures. Its lower bound reaches a little more than halfway to the cavity floor but mean reverse velocities are still present within it.

A sample pulse-burst PIV velocity field sequence is shown in Fig. 3 at Mach 0.8, offering nine snapshots extracted from a 10.2 ms burst of 386 velocity fields acquired at 37.5 kHz. Vectors show the in-plane velocity fluctuations superposed on a color contour plot of the streamwise velocity component; white line contours portray the vorticity magnitude exceeding a minimum threshold to emphasize the strongest regions of shear and turbulent eddies. In each figure, the positions of the cavity walls coincide with the axes and are shaded gray. The figure provides every third or fourth frame rather than successive frames to illustrate a longer-duration sequence of events. The initial time is arbitrary, set to the first vector field in the burst.

Figure 3 shows a sequence of events leading to a strong ejection event at the aft end of the cavity. The first frame, at t=2000 μs, represents a fairly benign instance of cavity turbulence. Vorticity aligned with the shear layer is approximately horizontal, recirculation velocities are mild, and no large coherent structures are evident. In the second frame shown (actually three time steps later) where t=2080 μs, an upswelling has begun in the shear layer near x=40 mm, initiated by the intersection of a recirculation motion and a vortical motion within the shear layer. Its growth continues into subsequent frames. At t=2187 μs, a broader extent of the shear layer is lifting and combines with an increasing magnitude of reverse velocities below it to generate a substantial vortex that is evident in both the velocity vectors and the vorticity contours. The upswell and the vortex continue to grow and move downstream while the recirculation magnitudes intensify in Fig. 3d at t=2294 μs. At this point, the upwards bulge in the shear layer dominates the middle of the cavity. At t=2400 μs, strengthening reverse velocities support the upswell and continue to push it outward as it moves downstream.

As Fig. 3 continues into its second page, the leading edge of the upswell approaches the cavity's aft end at t=2507 μs then begins to exit the cavity at t=2587 μs. This is the beginning of the ejection event in Fig. 3g, with the largest extent of the upswelling yet to reach the aft end. A large bulge extends from x=65 mm to x=110 mm with vorticity marking boundaries as it shears against both the freestream and the recirculation region. Finally, the large uprising coherent structure nears the aft wall at t=2667 μs, while the upstream end of the shear layer has returned to a more horizontal alignment than it possessed earlier in this sequence. As the ejection event completes in Fig. 3i, the recirculation region has shifted upstream with lower speed fluid evident deep into the aft end of the cavity. Fluid can be observed exiting the cavity and drawing with it fluid from inside the cavity near the aft wall. The sequence as a whole exemplifies how events within the recirculation region and the shear layer may interact to create a large-scale turbulent structure that induces a strong dynamic event at the aft end of the cavity. It also shows that the recirculation region can briefly shift upstream, at least within the extent of the cavity captured by the field of view. Since the velocity field does not reach the cavity floor, any motion nearer the floor may contradict the vectors available.

Power Spectra

Each of the PIV vectors can be considered a temporal velocity signal and thus may be analyzed for frequency content by calculating the power spectra of the velocity fluctuations. A power spectral density (PSD) was generated for each burst of data, then the 250-burst data set was averaged to produce low-noise spectra. Three points in the flow were selected to represent different gross flowfield features. One was placed upstream in the shear layer at x=25.3 mm, y=1.5 mm and another was placed in the middle of the shear layer at x=63.5 mm, y=0.4 mm. (The reason for the slightly elevated upstream position will become apparent subsequently and the even smaller elevation of the middle position simply reflects the closest vector to y=0.) The third point is located within the recirculation region near the aft end of the cavity, x=101.8 mm, y=-13.1 mm.

The three velocity spectra are given in Fig. 4 for Mach 0.8, where Fig. 4a shows the streamwise component and Fig. 4b the vertical component. Also presented in Fig. 4 is a PSD of the pressure fluctuations recorded by a high-frequency pressure sensor (Kulite XCQ-062) installed in the aft cavity wall at y=-10.7 mm on spanwise center and sampled at 200 kHz. Pressure and velocity spectra are necessarily plotted on separate axes, whose relative scaling is arbitrarily selected to ease comparisons of the resonances. Four acoustic tones are clearly seen in the pressure spectrum, corresponding to the first four Rossiter tones in the cavity. The mode 4 tone at about 3.2 kHz shows a bifurcation and then an additional narrow tone at about 3.8 kHz. Careful investigation suggests that these are residual effects of wind tunnel wall interference and the tone associated solely with cavity resonance is the peak at 3.25 kHz [25]. The velocity peaks are broadened in comparison with the pressure peaks – most apparent for mode 2 – because the velocity PSD's were computed using a frequency resolution of 100 Hz limited by the 10.2 ms burst duration, whereas the much longer record length of the pressure data allowed a resolution of 10 Hz.

Most of the pressure peaks are matched in the velocity spectra, but their presence varies depending upon resonance mode and choice of velocity component. Mode 1 is not evident in any of the three velocity points. Mode 2, conversely, is most commonly present. It can be seen for the streamwise component for all three points and in at least two of the points for the vertical component; only the point within the recirculation region in Fig. 4b appears not to show evidence of mode 2, though it may be weakly present. Modes 3 and 4 are observed in the velocity spectra as well but inconsistently depending upon the point and component that is examined. The bifurcated nature of mode 4 appears to be reflected in the velocity spectra by broadened peaks, and the tunnel mode at 3.8 kHz has some presence in the velocity data as well. In all cases, spectral peaks in the velocity data well match the frequencies found in the pressure spectrum.

Clearly, the various acoustic resonances are not uniformly present throughout the velocity field. To examine the spatial distribution of each resonance tone, similar spectral information is available for every velocity vector recorded and may be used to identify locations where acoustic loading is most intense. To this purpose, the PSD amplitudes are extracted at four frequencies corresponding to each mode and are shown in Fig. 5, where Figs. 5a – 5d show PSD amplitudes of the streamwise component and Figs. 5e – 5h for the vertical component. Each of the four modes is given respectively.

It is immediately evident from Fig. 5 that mode 1 is concentrated within the recirculation region whereas modes 2 through 4 are localized in the shear layer. This sort of spatial variation in resonance amplitude has previously been observed by Rockwell and Kniseley [13] and Basley et al [9] as well as the simulations of Larchevêque et al [34]. Differences also may be observed in the streamwise component versus the vertical component. Mode 1 resides lower in the recirculation region for the vertical component as compared to the streamwise component. As the mode number increases, the PSD energy in the vertical component is restricted to a narrower strip near the center of the shear layer, but this is not the case in the streamwise direction. The streamwise component also appears to have a short and thin but intense concentration of energy immediately downstream of the cavity leading edge, which is not manifest in the vertical component. The core of this spot is elevated slightly above the cavity lip, which is the reason for the raised position of the upstream point in Fig. 4. Excepting mode 1, peak amplitudes are fairly similar for each component though not distributed identically.

However, a comparison of the spatial distributions in Fig. 5 with the point PSD's in Fig. 4 reveals additional complexity. No mode 1 peak is observed in the velocity point PSD's in Fig. 4 but clearly large energy may be found in the amplitude plots of Figs. 5a and 5e. This implies that the mode 1 resonance, clearly present in the pressure spectrum, is subsumed by turbulent fluctuations in the velocity spectra. The elevated point PSD representing the recirculation region suggests turbulent activity across a broad range of low-frequency motion, and therefore the amplitudes in Figs. 5a and 5e are more representative of this than they are of the acoustic resonance that nevertheless is present. Similarly, the mid-length point in the shear layer does not show a mode 3 peak in Fig. 4a but clearly there is elevated energy in the corresponding amplitude plot of Fig. 5b; this again suggests the dominance of turbulent activity over the acoustic resonance in the velocity spectra at this frequency. This is the case in the streamwise component only, whereas the vertical component of the point PSD's clearly shows resonance peaks exceeding the turbulent fluctuations, and hence the amplitudes in Fig. 5g do reflect resonance energy. Regardless of the source of energy – turbulence or acoustic resonance – Fig. 5 uses the unique capabilities of pulse-burst PIV to map the loading environment within the cavity at specific frequencies.

Though Figs. 4 and 5 show data only for Mach 0.8, results at the other two Mach numbers are substantially similar, differing in peak amplitude for each resonance mode but not in spatial character. Hence, they are omitted for brevity.

Spatio-Temporal Correlations

The spatial scales of the coherent structures responsible for the resonance modes also may be found from the pulse-burst PIV data. The temporal signal of a selected reference vector was correlated with each of the other vectors present in the PIV measurement. This produces cross-correlation fields with both spatial and temporal character that can track how correlation peaks and anti-peaks move through space and time as resonance occurs in the cavity. In the present case, the reference velocity signal was chosen as nominally x=25.4 mm, y=0 mm (actually displaced by a fraction of a mm to align with the nearest vector location) to represent the initial activity of the shear layer. Cross-correlations were computed for the entire duration of each of the 250 bursts, then averaged into a single resulting signal.

Figure 6 shows the resulting correlation fields for Mach 0.8, with the streamwise component given in Figs. 6a though 6e and the vertical component in Figs. 6f through 6j. The initial time in Figs. 6a and 6f reveals a primary correlation peak aligned approximately horizontal for u and vertical for v, in each case with a long axis of about 20-30 mm in length. These suggest the length scale of coherent structures in the shear layer. Anti-correlations are seen as well, separated by about 20 mm from the primary peak, and another weak correlation peak is seen farther downstream moving beyond the field of view. Entire movies of the cross-correlation are produced to match the frames of the pulse-burst PIV data, but time steps have been selected to represent key instances in the evolution of the flow. Since Mach 0.8 resonance is dominated by the second mode at 1520 Hz, a full period of resonance can be expected to last 658 μs. Figure 6b shows the cross-correlation field 1/4 of a period later for the u component, Fig. 6c shows it 1/2 a period later, and Fig. 6d a full period later (within rounding error). Corresponding time delays for the v component are given in Figs. 6g, 6h, and 6i. These show the correlated and anti-correlated coherent structures convecting downstream and moving vertically out of the field of view, while their correlation strengths weaken. Correlation peaks are cut to about a third of their maximum value after only one period. A final frame is shown four periods after the initial time at t=2640 μs and correlations have become defuse and weak.

The principal reason the correlation fields weaken so quickly is that some or all of the four resonances may be active simultaneously, plus broadband turbulence occurring as well. These effects interfere with one another and cloud any attempt to detect coherent motions associated with single resonances over significant durations. Fortunately, a solution may be implemented by first bandpass filtering the pulse-burst PIV data for specific resonance modes, then computing the cross-correlations. The filtering was accomplished using an FFT-based filter for each of the four resonance modes observed in Fig. 4, at frequencies of 620, 1520, 2380, and 3250 Hz, respectively, for Mach 0.8. A Blackman windowed-sinc filter was employed with a filter bandwidth (full width) of 300 Hz, approximately matching the peak broadening of the velocity signal.

The filtered cross-correlations are shown in Figs. 7 through 10, representing modes 1 through 4, respectively. Mach 0.8 data are shown and here only the vertical velocity component is considered, which is the more useful of the two because it better aligns to the horizontal orientation of the field of view and the principal convection direction. Mode 1 exhibits different behavior than modes 2 through 4 and therefore will be discussed subsequently. Figure 8 shows the cross-correlations associated with mode 2, the strongest resonance and characteristic of the three higher modes. The same time steps are used as in Fig. 6 but with strikingly different outcome. A clear resonance wave is present. In this narrow frequency band, the correlation strength remains much greater with distance in both space and time. At the initial time step in Fig. 8a, more than one full period of the resonance can be seen and the magnitude of the correlation remains near its maximum at its second peak near x=100 mm with a value of R=0.8. This is in contrast to the unfiltered data of Fig. 6 where the downstream positive correlation was scarcely visible. Similarly, as the coherent structures march through time, they retain their strength and spatial coherence. Even four periods later in Fig. 8e, correlation peak amplitudes of $R = \pm 0.6$ are found. Modes 3 and 4 in Figs. 9 and 10 behave analogously, remaining strongly correlated in both space and time.

The spatial characteristics of the resonance modes are a function of the resonance frequency. As the mode number increases from Fig. 8 to Figs. 9 and 10, the wavelength of the disturbance shortens (and therefore the time steps are adjusted so that each figure continues to represent phases of 1/4, 1/2, 1, and 4 periods following the initial time). The spatial scale of the coherent structures also shortens as the mode increases. The spacing between the structures is not uniform; their separation increases as they convect downstream. It also is notable that the structures tend to drift outward from the cavity despite a reference point located on the shear layer centerline.

Cross-correlations also were computed using different locations along the shear layer centerline as the reference velocity. Reference locations of x=50.8, 76.2, and 101.6 mm, all at y=0 mm, were examined as well and found to be substantially similar to Figs. 8-10. The behavior of the coherent structures is not a function of the streamwise position of the reference velocity.

Mode 1 behavior is entirely different from modes 2 through 4. Figure 7 shows no evidence of a correlated resonance wave in space. However, a standing wave does remain fixed on the reference location and can be observed to oscillate in time. It correlates over a length scale of about 40 – 50 mm but shows minimal additional positive or negative correlation downstream. Previous cavity investigations also have noted that mode 1 differs from higher modes and attribute this to the wavelength of the disturbance frequency exceeding the cavity length, which is not the case for higher mode numbers [19, 32]. An earlier study of the present flowfield also noted aberrant behavior for mode 1 based on an alternative analysis technique [23].

Since Fig. 5 shows the mode 1 resonance to concentrate in the recirculation region, the unusual behavior of the cross-correlation in Fig. 7 may be a result of the choice of reference velocity within the shear layer. An alternative reference velocity was selected within the recirculation region instead, located at x=101.6 mm, y=-10 mm, and cross-correlations based upon this reference point are shown in Fig. 11. As it turns out, this does nothing to change the flow behavior. Instead, the apparent standing wave is centered on the new reference point but still does not display any evidence of a spatially resonating wave. The scale of the coherence also remains consistent with Fig. 7. This suggests that differing nature of mode 1 is not a result of a spatial distribution of cavity resonance properties and in fact is consistently exceptional across the entire cavity.

Spatio-temporal cross-correlations were found for the Mach 0.6 and 0.94 data sets in the same fashion as has been conducted for Mach 0.8. Results were consistent with Figs. 7-10, other than the expected differences due to changing freestream velocity and resonance peak frequencies. Inclusion of figures for these additional Mach numbers would not provide value.

The spacing and convection velocities of the coherent structures in Figs. 8-10 may be determined quantitatively from the cross-correlation fields. A simple algorithm was crafted in which the correlation peaks, both positive and negative, were located in space and time and then tracked as they convect downstream. Sub-grid accuracy was obtained by fitting a second-order polynomial in the vicinity of each peak and extracting its peak location. The streamwise spacing then was easily derived from these peak positions as a function of the streamwise location of the first of two successive coherent structures. The convection velocity was found by tracking the peak position of a structure across five time steps, then calculating its derivative from these five positions.

Figure 12 shows the spacing between coherent structures measured in this fashion. Since successive structures are anti-correlated, these distances represent half of a resonance period. Distances are measured purely in x because resonance is aligned to this longitudinal direction. At this juncture in the data analysis, it becomes valuable to examine all three Mach numbers. In all cases and for all modes, the separation between successive coherent structures increases with downstream distance and decreases as the mode number rises. This was qualitatively evident from the cross-correlation fields of Figs. 8-10. Structure separations increase with rising Mach number, which is intuitive due to the larger freestream velocity. The drop in spacing nearer the aft end of the cavity is artificial, occurring as structures move beyond the field of view and a peak is falsely located near the edge of the vector field. Also, the large undulation in the mode 3 curve for Mach 0.94 is most likely an artifact of the data processing algorithm.

In Fig. 13, the convection velocities are displayed for the three Mach numbers. The convergence of the cross-correlation fields coupled with errors in locating the correlation peaks leads to considerable scatter in the data. Yet two observations may be reasonably discerned despite the scatter. First, the convection velocity rises with downstream distance, matching the behavior of the structure spacing of Fig. 12. Secondly, and somewhat more tenuously, the convection velocity appears to be the same for all three modes. Another useful observation that may be made is that the data points do not merely scatter, but group together in tendrils. This is particularly evident in the Mach 0.94 data. These features almost certainly are an artifact of the data reduction method used to locate the correlation peaks and estimate the spacing and velocity of the coherent structures. Amongst the future work planned for continued analysis of the present data set is an increased sophistication to this algorithm.

Given the availability of the spacing of the coherent structures and their convection velocities, characteristic frequencies are readily computed by $f = v_{conv}/2\Delta x$. If these coherent structures are responsible for the cavity resonance modes, the calculated frequencies ought to match the resonance frequencies measured by the pressure sensors. Figure 14 shows these characteristic frequencies derived from the coherent structures for each Mach number and each of the three higher acoustic modes. Again, the scatter in the data limits the precision to which a comparison can be made. Still, it is reasonable to suggest that the structure frequencies are consistent with the pressure-based resonance frequencies. Certainly, the higher modes result in higher estimated frequencies. The bulk of the data points for each mode appear to reside at slightly lower frequencies than the pressure-determined frequencies, but plausible agreement may be inferred. No variation with streamwise distance is evident.

It is possible that the consistency of the calculated frequencies is an artifact of the data processing, though in this case not due to the imprecise location of the correlation peaks. A bias in the calculation of the properties of the coherent structures may occur due to the use of a specific frequency band. If the frequency of the disturbance were to change with downstream distance, it would move outside the filter band and be removed from the analysis. However, this is impossible to assess from the current data reduction algorithm. Figure 14 clearly shows that the scatter in the estimated frequencies greatly exceeds the 300 Hz bandwidth of the measurements. Future refinement of the analysis techniques will be required prior to studying the stability of the characteristic frequencies.

In summary of Figs. 12-14, despite the data scatter and the limitations of the current data processing algorithm, some conclusions may be drawn concerning the coherent structures corresponding to each resonance mode (excepting the contrary mode 1). The spacing between successive coherent structures decreases for higher resonance modes, which has been observed previously [10, 16, 19]. This spacing increases with downstream distance. The convection velocity appears to be identical for all resonance modes, but it too increases with downstream distance. Both the original Rossiter equation [11] and Heller and Bliss's modification of it [12] assume a convection velocity identical for all modes and constant in space. The present data show that the latter is not accurate, but these two parameters vary together such that the resulting resonance frequency remains stable.

One of the key questions that has not yet been answered is whether the convection velocity varies with vertical position. Changing the location of the reference velocity for the cross-correlations to different heights within the shear layer may reveal a positional dependence to the convection velocity and, presumably, the spacing of the coherent structures. This remains for future analysis of the present data set.

Conclusions and Future Work

Pulse-burst PIV has been used to acquire time-resolved data at 37.5 kHz of the flow over a finite-width rectangular cavity at Mach numbers of 0.6, 0.8, and 0.94. This variant of time-resolved PIV is necessary to obtain the temporal component of the velocity field in a high-speed ground testing facility. Data were acquired in the streamwise plane along the spanwise center of the cavity to explore the characteristics of the acoustic resonance present in the flowfield. Power spectra of the PIV data reveal four resonance modes that match the frequencies detected simultaneously using high-frequency pressure sensors installed in the cavity walls. The velocity resonances, however, are not uniformly present in the flowfield and instead show spatial dependence. The lowest frequency acoustic mode is active within the recirculation region of the cavity whereas the three higher modes are concentrated within the shear layer.

Spatio-temporal cross-correlations reveal the dynamics of the coherent structures in the velocity field and their relationship with the resonance modes. However, because some or all of the resonance modes are active simultaneously while broadband turbulence is present as well, competition between these effects clouds any attempt to detect coherent motions associated with single resonances. This challenge was overcome by first bandpass filtering the velocity data for specific resonance frequencies and then computing the cross-correlations, a procedure made possible by the temporal information supplied by the pulse-burst PIV technique. The low-frequency acoustic mode behaves differently than the three higher modes because it is associated with a characteristic wavelength exceeding the cavity length. It shows properties of a standing wave but no acoustic wave correlated in space. In contrast, the higher resonance modes are associated with the coherent structures in the velocity field that convect downstream and persist for many periods of resonance. The spacing between successive coherent structures decreases for higher resonance modes and increases as structures convect downstream. The convection velocity appears to be identical for all resonance modes, but it too increases with downstream distance. These two parameters vary together such that the resulting resonance frequency remains stable. This is in contrast to the well-known Rossiter equation, which predicts cavity resonance frequencies assuming a convection velocity constant in space.

Data analysis is ongoing. In particular, it has not yet been determined whether the properties of the coherent structures responsible for resonance possess a dependence on the vertical position within the shear layer. The current, tentative conclusions regarding the spacing of these coherent structures and their convection velocity are partially obscured by imprecision in the data reduction of the correlation fields, and a more sophisticated analysis algorithm is under development. Implementation of dynamic mode decomposition (DMD) also is intended as an alternative means of detecting spatially coherent structures associated with the various resonance modes. Finally, the simultaneous data acquired using high-frequency pressure sensors presents an opportunity to correlate the instantaneous pressure with the resonance properties revealed by the velocity field. These additional data analysis approaches, coupled with the current results, will more completely and confidently describe the velocity field dynamics responsible for the acoustic resonances that dominate the behavior of flow over a cavity.

Acknowledgments

The authors would like to thank Srinivasan Arunajatesan, Matthew Barone, and Katya Casper, all of Sandia, for numerous fruitful conversations regarding cavity resonance and their helpful comments on the data and their interpretation.

References

[1] Wernet, M., "Temporally Resolved PIV for Space-Time Correlations in Both Cold and Hot Jet Flows," *Measurement Science and Technology*, Vol. 18, No. 5, 2007, pp. 1387-1403.

[2] Brock, B., Haynes, R. H., Thurow, B. S., Lyons, G., and Murray, N. E., "An Examination of MHz Rate PIV in a Heated Supersonic Jet," AIAA Paper 2014-1102, January 2014.

[3] Miller, J. D., Michael, J. B., Slipchenko, M. N., Roy, S., Meyer, T. R., and Gord, J. R., "Simultaneous High-Speed Planar Imaging of Mixture Fraction and Velocity using a Burst-Mode Laser," *Applied Physics B*, Vol. 113, 2013, pp. 93-97.

[4] Miller, J. D., Gord, J. R., Meyer, T. R., Slipchenko, M. N., Mance, J. G., and Roy, S., "Development of a Diode-Pumped, 100-ms Quasi-Continuous Burst-Mode Laser for High-Speed Combustion Diagnostics," AIAA Paper 2014-2524, June 2014.

[5] Beresh, S. J., Kearney, S. P., Wagner, J. L., Guildenbecher, D. R., Henfling, J. F., Spillers, R. W., Pruett, B. O. M., Jiang, N., Slipchenko, M., Mance, J., and Roy, S., "Pulse-Burst PIV in a High-Speed Wind Tunnel," *Measurement Science and Technology*, Vol. 26, No. 9, 2015, pp. 095305.

[6] Haigermoser, C., Vesely, L., Novara, M., and Onorato, M., "A Time-Resolved Particle Image Velocimetry Investigation of a Cavity Flow with a Thick Incoming Turbulent Boundary Layer," *Physics of Fluids*, Vol. 20, 2008, pp. 105101.

[7] Bian, S., Driscoll, J. F., Elbing, B. R., and Ceccio, S. L., "Time Resolved Flow-Field Measurements of a Turbulent Mixing Layer over a Rectangular Cavity," *Experiments in Fluids*, Vol. 51, No. 1, 2011, pp. 51-63.

[8] Liu, X., and Katz, J., "Vortex-Corner Interactions in a Cavity Shear Layer Elucidated by Time-Resolved Measurements of the Pressure Field," *Journal of Fluid Mechanics*, Vol. 728, 2013, pp. 417-457.

[9] Basley, J., Pastur, L. R., Lusseyran, F., Faure, T. M., and Delprat, N., "Experimental Investigation of Global Structures in an Incompressible Cavity Flow using Time-Resolved PIV," *Experiments in Fluids*, Vol. 50, No. 4, 2011, pp. 905-918.

[10] Gueniat, F., Pastur, L., and Lusseyran, F., "Investigating Mode Competition and Three-Dimensional Features from Two-Dimensional Velocity Fields in an Open Cavity Flow by Modal Decompositions," *Physics of Fluids*, Vol. 26, No. 8, 2014, pp. 085101.

[11] Rossiter, J. E., "Wind-Tunnel Experiments on the Flow Over Rectangular Cavities at Subsonic and Transonic Speeds," Aeronautical Research Council Reports and Memoranda, October 1964.

[12] Heller, H. H., and Bliss, D. B., "The Physical Mechanism of Flow Induced Pressure Fluctuations in Cavities and Concepts for Suppression," AIAA Paper 75-491, March 1975.

[13] Rockwell, D., and Knisely, C., "The Organized Nature of Flow Impingement upon a Corner," *Journal of Fluid Mechanics*, Vol. 93, No. 3, 1979, pp. 413-432.

[14] Gharib, M., and Roshko, A., "The Effect of Flow Oscillations on Cavity Drag," *Journal of Fluid Mechanics*, Vol. 177, 1987, pp. 501-530.

[15] Forestier, N., Jacquin, L., and Geffroy, P., "The Mixing Layer over a Deep Cavity at High-Subsonic Speed," *Journal of Fluid Mechanics*, Vol. 475, 2003, pp. 101-145.

[16] Murray, N. E., and Ukeiley, L. S., "Flow Field Dynamics in Open Cavity Flows," AIAA Paper 2006-2428, May 2006.

[17] Murray, N. E., and Ukeiley, L. S., "Modified Quadratic Stochastic Estimation of Resonating Subsonic Cavity Flow," *Journal of Turbulence*, Vol. 8, No. 53, 2007, pp. 1-23.

[18] Zhang, K., and Naguib. A., "Effect of Finite Cavity Width on Flow Oscillation in a Low-Mach-Number Cavity Flow," *Experiments in Fluids*, Vol. 51, No. 5, 2011, pp. 1209-1229.

[19] Kegerise, M., Spina, E. F., Garg, S., and Cattafesta, L. N., "Mode-Switching and Nonlinear Effects in Compressible Flow over a Cavity," *Physics of Fluids*, Vol. 16, No. 3, 2004, pp. 678-687.

[20] Kang, W., Lee, S. B., and Sung, H. J., "Self-Sustained Oscillations of Turbulent Flows over an Open Cavity," *Experiments in Fluids*, Vol. 45, No. 4, 2008, pp. 693-702.

[21] Beresh, S. J., Wagner, J. L., Pruett, B. O., Henfling, J. F., and Spillers, R. W., "Supersonic Flow over a Finite-Width Rectangular Cavity," *AIAA Journal*, Vol. 53, No. 2, 2014, pp. 296-310.

[22] Beresh, S. J., Wagner, J. L., Henfling, J. F., Spillers, R. W., and Pruett, B. O. M., "Width Effects in Transonic Flow over a Rectangular Cavity," *AIAA Journal*, Vol. 53, No. 12, 2015, pp. 3831-3834.

[23] Wagner, J. L., Casper, K. M., Beresh, S. J., Henfling, J. F., Spillers, R. W., and Pruett, B. O. M., "Relationship between Acoustic Tones and Flow Structure in Transonic Rectangular Cavity Flow," AIAA Paper 2015-2937, June 2015.

[24] Wagner, J. L., Beresh, S. J., Casper, K. M., DeMauro, E. P., Arunajatesan, S., Henfling, J. F., and Spillers, R. W., "Relationship between Transonic Cavity Tones and Flowfield Dynamics using Pulse-Burst PIV," to be presented at the AIAA Science and Technology Forum, January 2016.

[25] Wagner, J. L., Casper, K. M., Beresh, S. J., Henfling, J. F., Spillers, R. W., and Pruett, B. O. M., "Mitigation of Wind Tunnel Wall Interactions in Subsonic Cavity Flows," *Experiments in Fluids*, Vol. 56, No. 3, 2015, pp. 59.

[26] Slipchenko, M. N., Miller, J. D., Roy, S., Gord, J. R., Danczyk, S. A., and Meyer, T. R., "Quasi-Continuous Burst-Mode Laser for High-Speed Planar Imaging," *Optics Letters*, Vol. 37, No. 8, pp. 1346-1348, 2012.

[27] Slipchenko, M. N., Miller, J. D., Roy, S., Gord, J. R., and Meyer, T. R., "All-Diode-Pumped Quasi-Continuous Burst-Mode Laser for Extended High-Speed Planar Imaging," *Optics Express*, Vol. 21, No. 1, pp. 681-689, 2013.

[28] Slipchenko, M. N., Miller, J. D., Roy, S., Meyer, T. R., Mance, J. G., and Gord, J. R., "100-kHz, 100-ms, 400-J Burst-Mode Laser with Dual-Wavelength Diode Amplifiers," *Optics Letters*, Vol. 39, No. 16, 2014, pp. 4735-4738.

[29] Beresh, S. J., Wagner, J. L., and Pruett, B. O. M., "Particle Image Velocimetry of a Three-Dimensional Supersonic Cavity Flow," AIAA Paper 2012-0030, January 2012.

[30] Grace, S. M., Dewar, W. G., and Wroblewski, D. E., "Experimental Investigation of the Flow Characteristics within a Shallow Wall Cavity for both Laminar and Turbulent Upstream Boundary Layers," *Experiments in Fluids* Vol. 36, No. 5, 2004, pp. 791-804.

[31] Ashcroft, G., and Zhang, X., "Vortical Structures over Rectangular Cavities at Low Speed," *Physics of Fluids*, Vol. 17, No. 1, 2005, pp. 015104.

[32] Murray, N., Sallstrom, E., and Ukeiley, L., "Properties of Subsonic Open Cavity Flow Fields," *Physics of Fluids*, Vol. 21, No. 9, 2009, pp. 095103.

[33] Crook, S. D., Lau, T. C. W., and Kelso, R. M., "Three-Dimensional Flow within Shallow, Narrow Cavities," *Journal of Fluid Mechanics*, Vol. 735, 2013, pp. 587-612.

[34] Larchevêque, L., Sagaut, P., Thien-Hiep, L., and Comte, P., "Large-Eddy Simulation of a Compressible Flow in a Three-Dimensional Open Cavity at High Reynolds Number," *Journal of Fluid Mechanics*, Vol. 516, 2004, pp. 265-301.

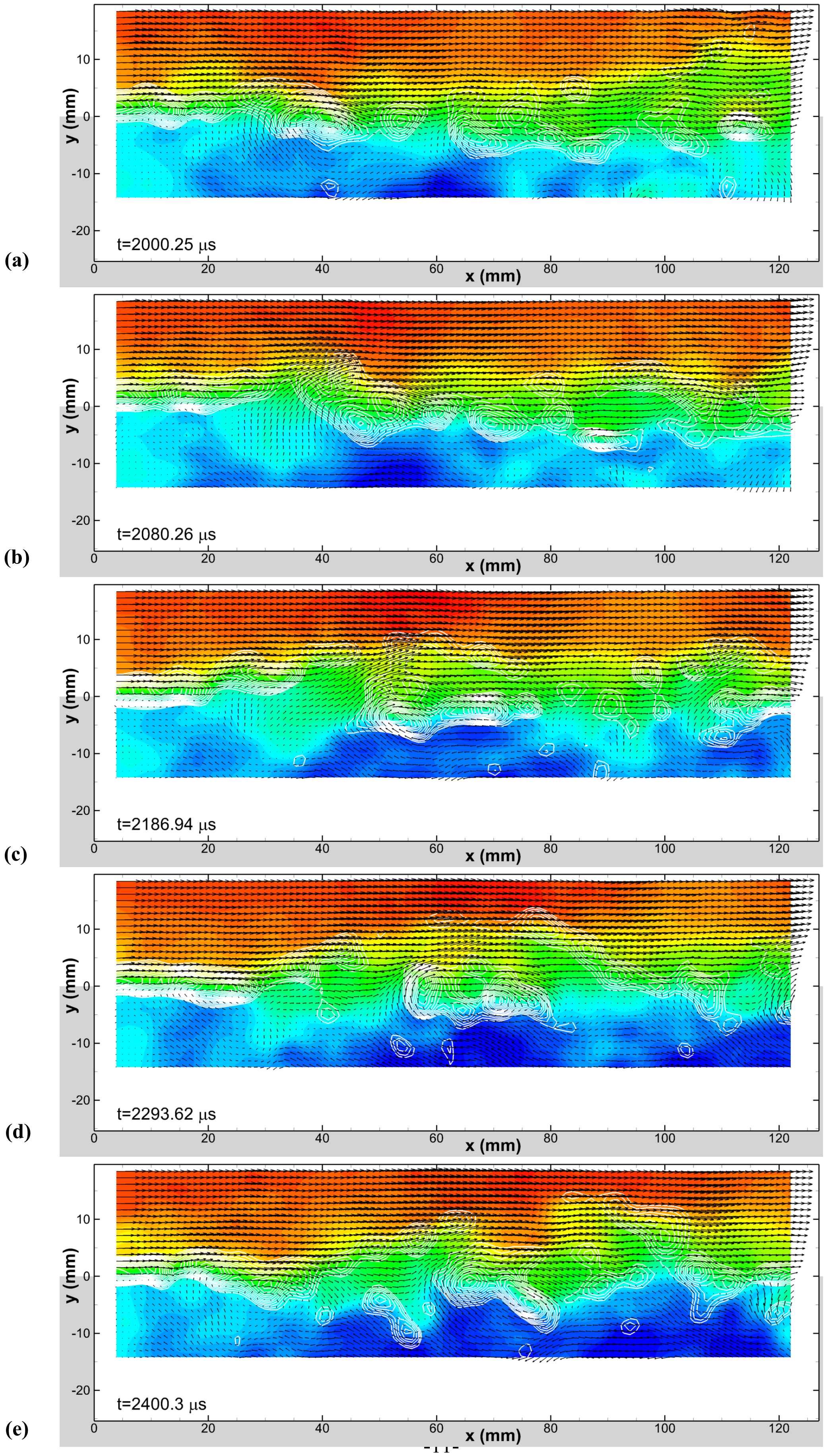

Fig. 3: Caption on subsequent page.

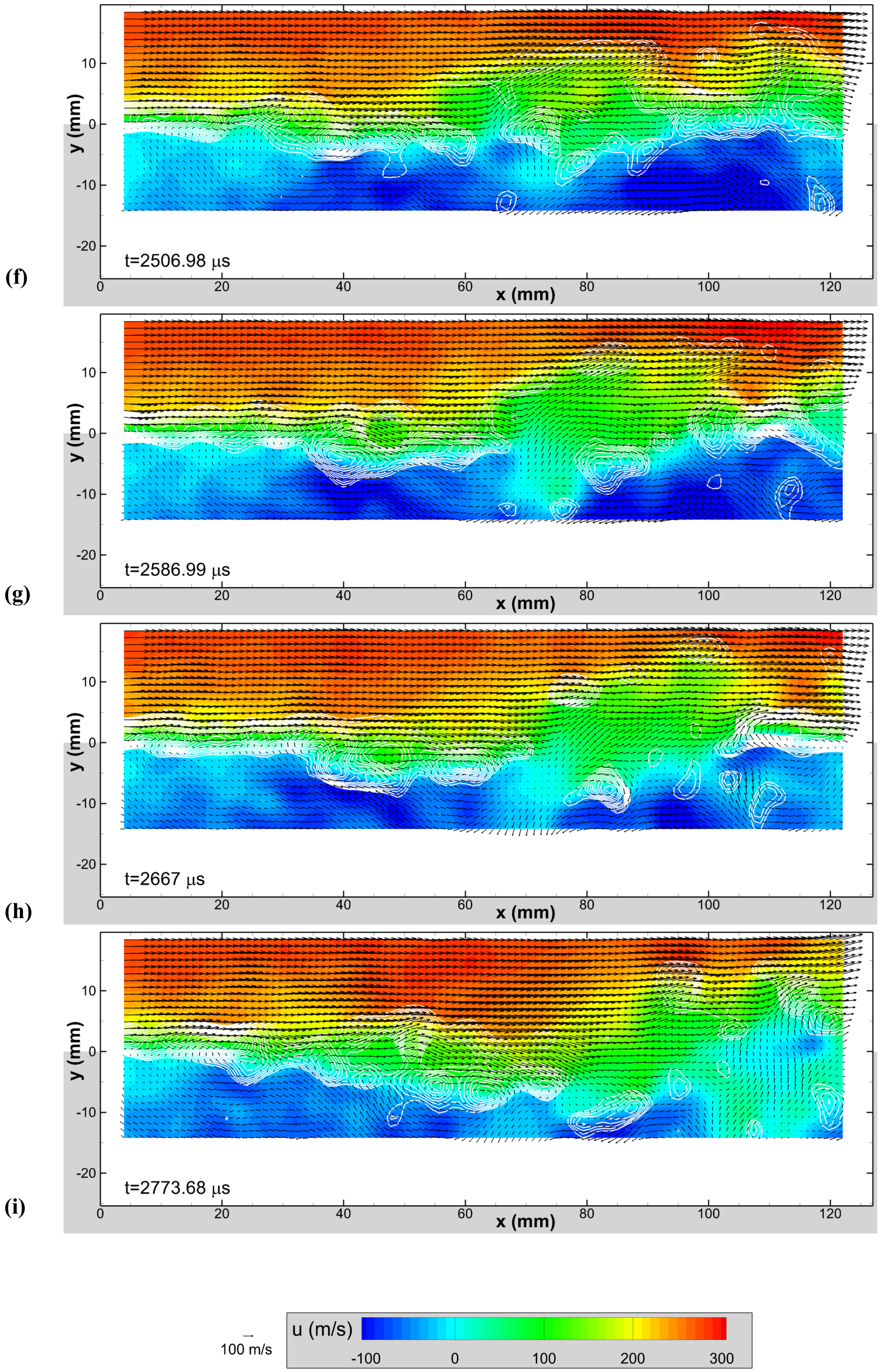

Fig. 3 (continued): Sequence of velocity fields extracted from a 10.2 ms burst of 386 velocity fields acquired at 37.5 kHz, for flow at Mach 0.8. Vectors show the in-plane velocities superposed on a color contour plot of the streamwise velocity component and white line contours of the vorticity magnitude exceeding a minimum threshold. Note the time sequence is not uniform, with every third or fourth vector field shown. Initial time is arbitrary from the start of the burst.

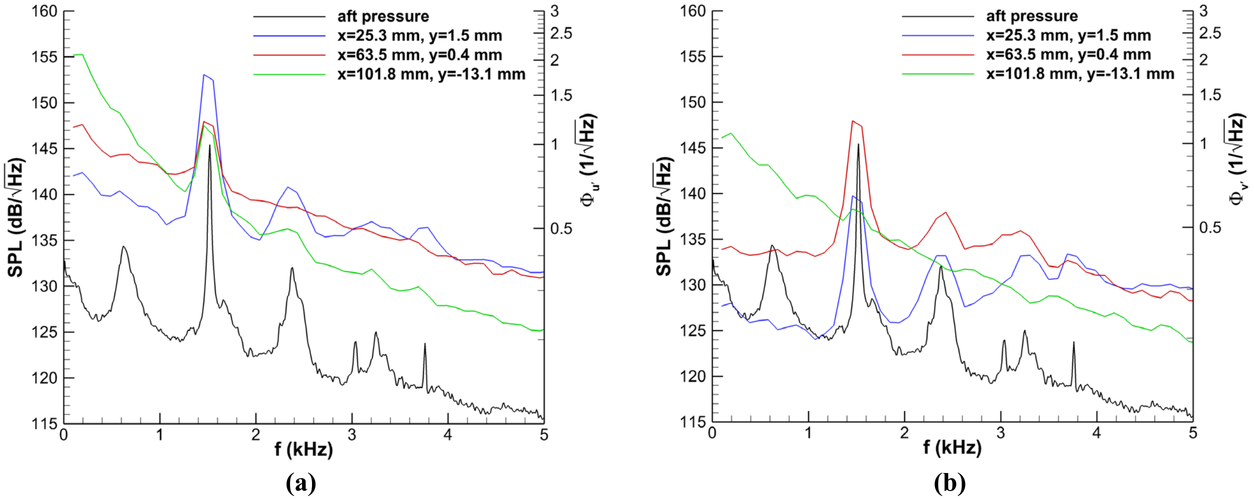

(a) (b)

Fig. 4: Power spectra of velocity fluctuations compared to the spectra of pressure fluctuations from a sensor in the aft cavity wall. Three velocity locations are shown: upstream in the shear layer (*x*=25.3 mm, *y*=1.5 mm), mid-length in the shear layer (*x*=63.5 mm, *y*=0.4 mm), and in the recirculation region (*x*=101.8 mm, *y*=-13.1 mm). Mach 0.8. (a) Streamwise component; (b) Vertical component.

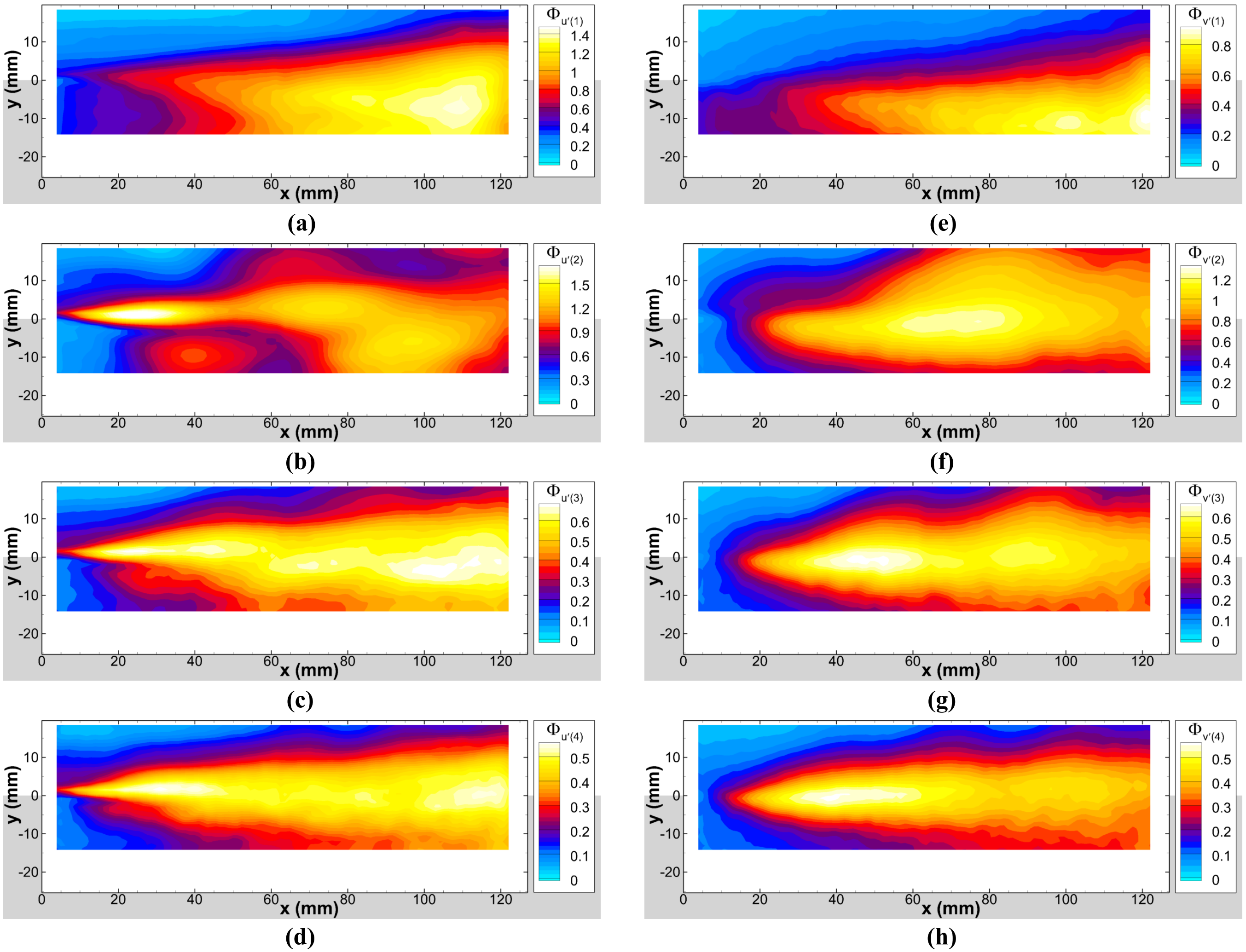

Fig. 5: Spatial distribution of power spectral density amplitudes (1/√Hz) of velocity fluctuations at each of the first four acoustic tones for Mach 0.8; (a) – (d): streamwise component; (e) - (h) vertical component.

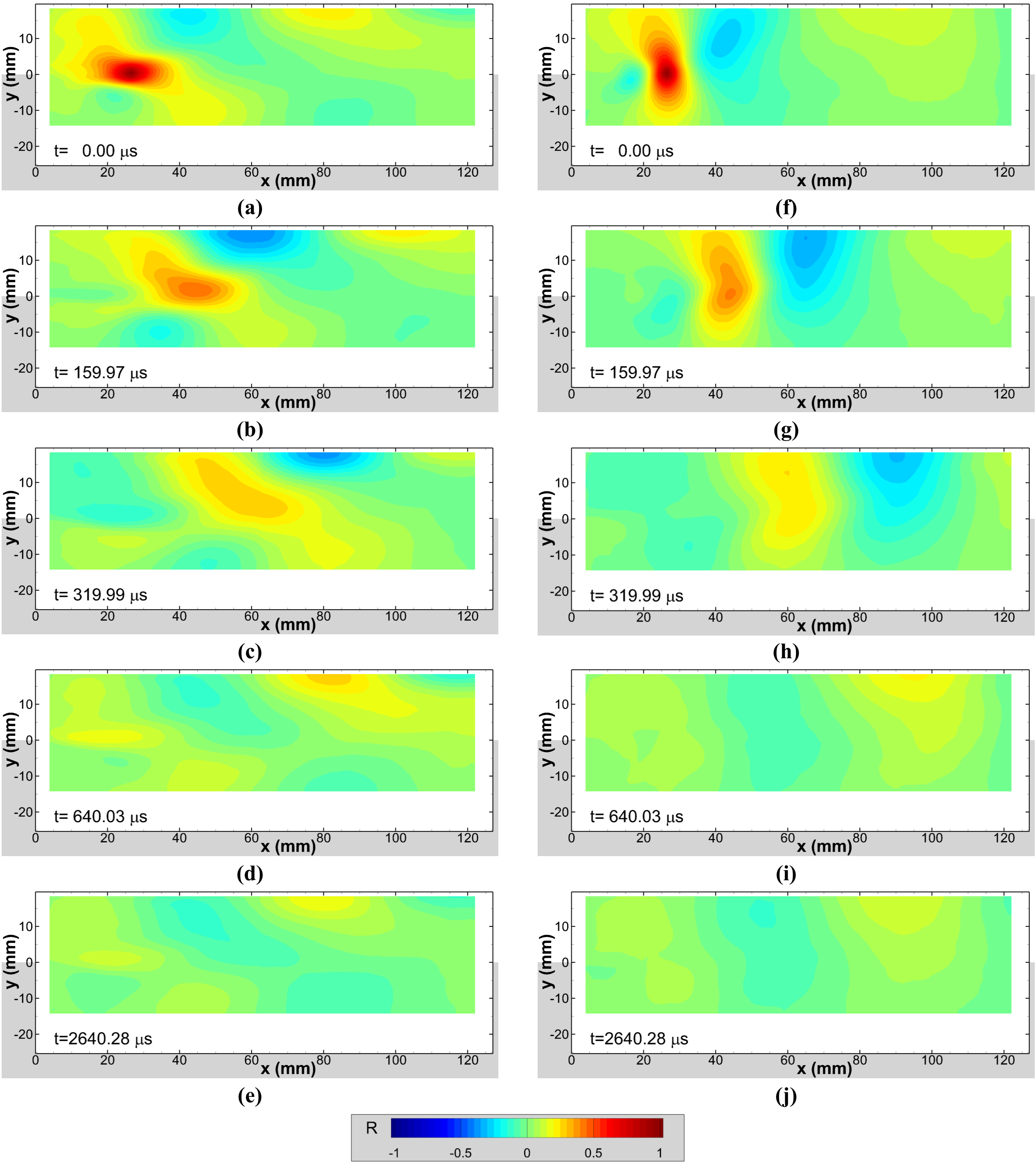

(a) (b) (c) (d) (e) (f) (g) (h) (i) (j)

Fig. 6: Spatio-temporal cross-correlations of the velocity field using a reference velocity at x=25.4 mm, y=0 mm for Mach 0.8; (a) – (e): streamwise component; (f) - (j) vertical component.

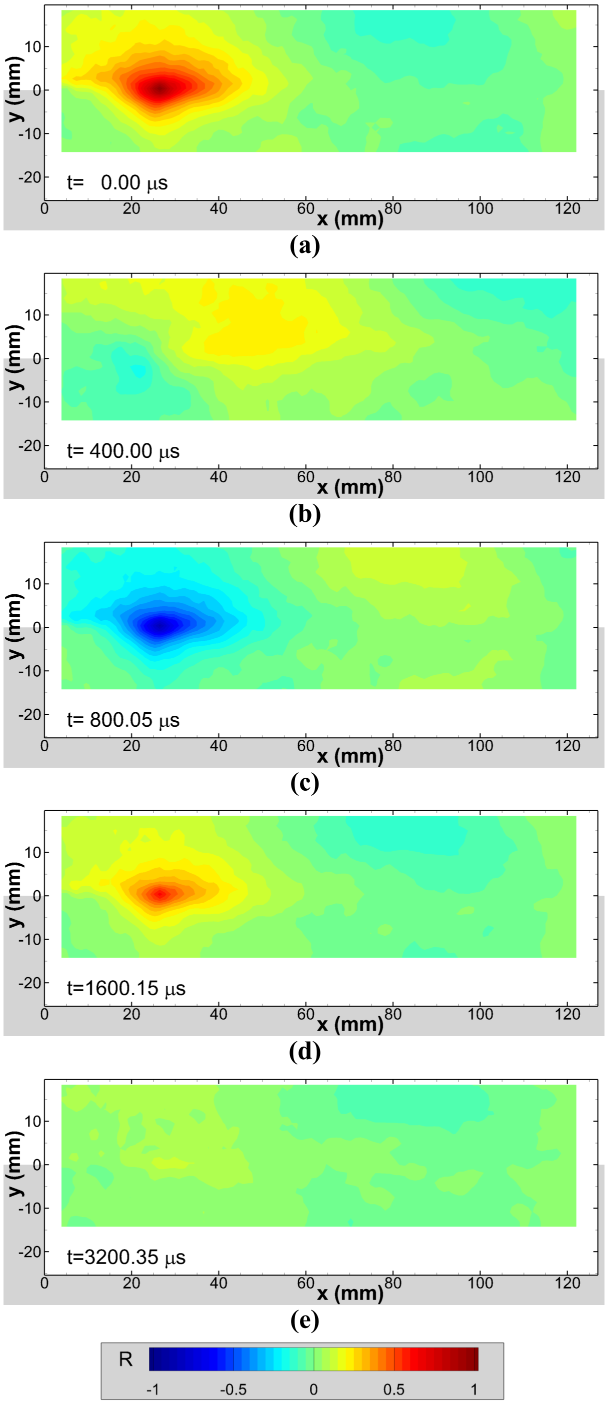

(a) (b) (c) (d) (e)

Fig. 7: Spatio-temporal cross-correlations of the vertical component of the velocity field filtered for the mode 1 resonance (620 Hz). Reference velocity at x=25.4 mm, y=0 mm; Mach 0.8.

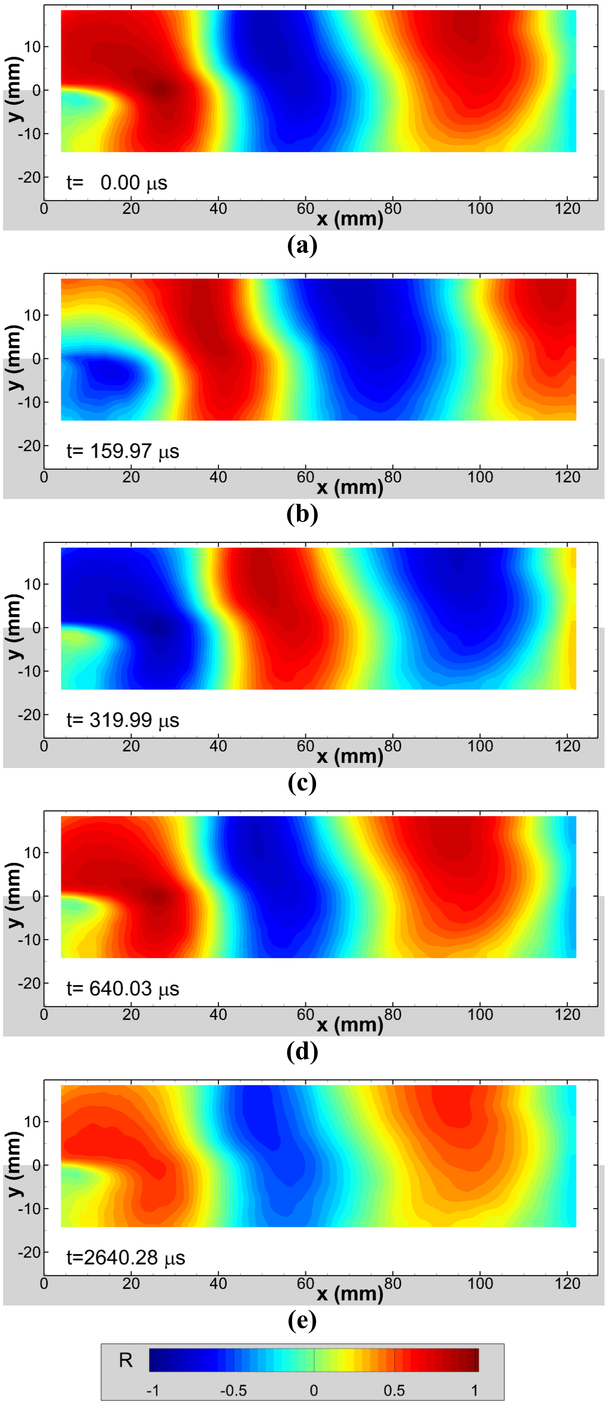

(a) (b) (c) (d) (e)

Fig. 8: Spatio-temporal cross-correlations of the vertical component of the velocity field filtered for the mode 2 resonance (1520 Hz). Reference velocity at x=25.4 mm, y=0 mm; Mach 0.8.

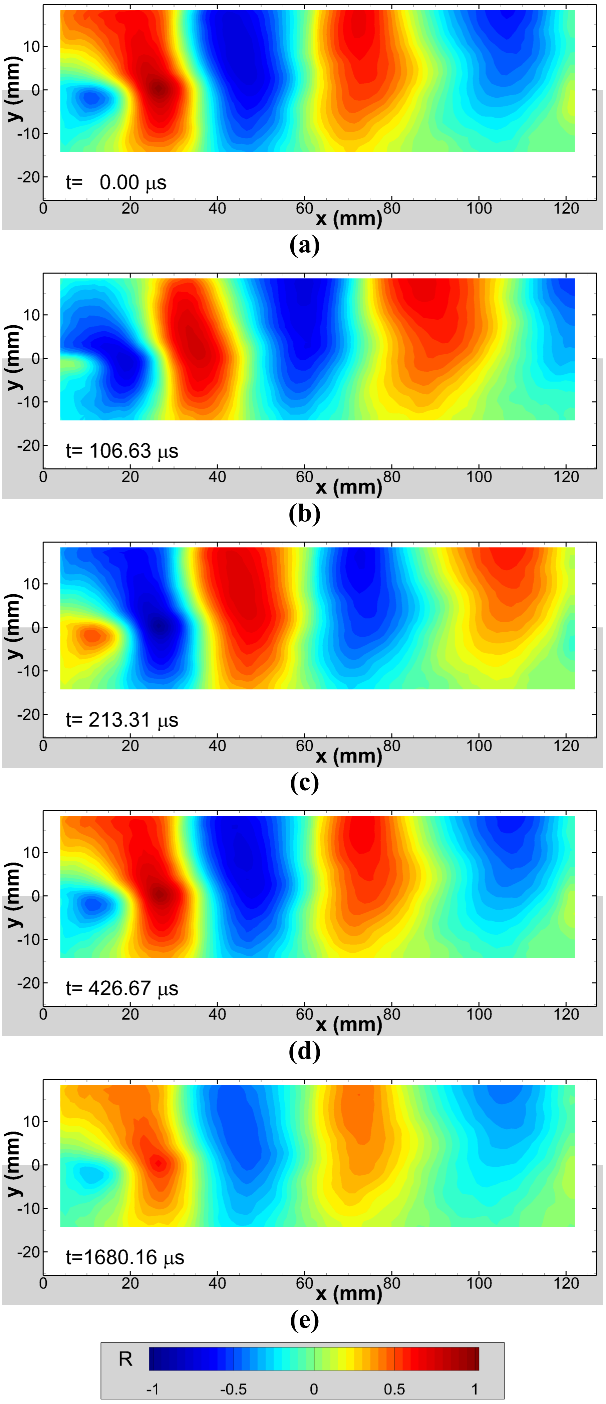

Fig. 9: Spatio-temporal cross-correlations of the vertical component of the velocity field filtered for the mode 3 resonance (2380 Hz). Reference velocity at *x*=25.4 mm, *y*=0 mm; Mach 0.8.

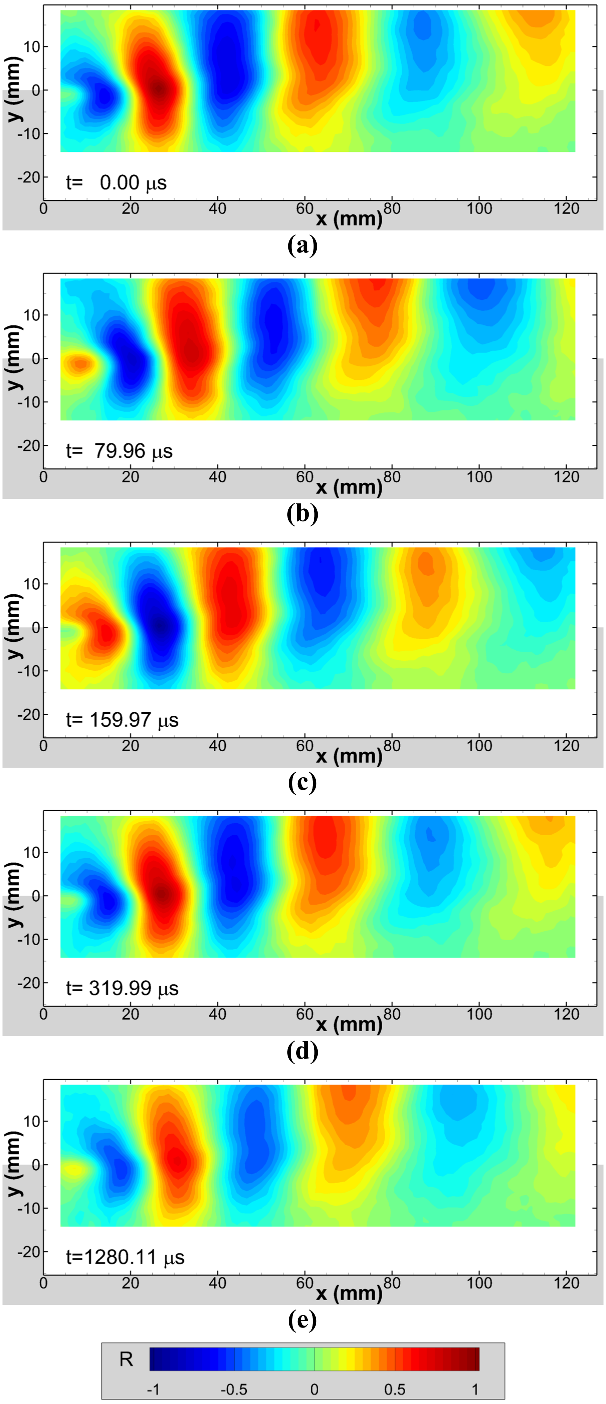

Fig. 10: Spatio-temporal cross-correlations of the vertical component of the velocity field filtered for the mode 4 resonance (3250 Hz). Reference velocity at *x*=25.4 mm, *y*=0 mm; Mach 0.8.

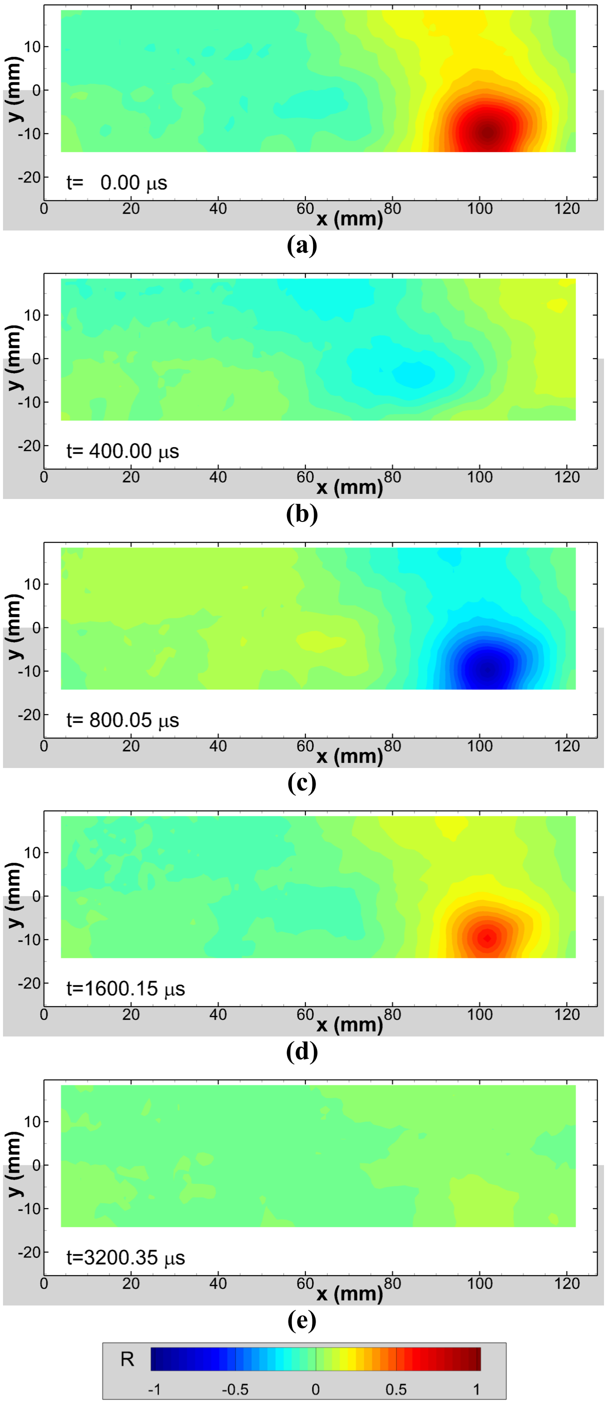

(a) (b) (c) (d) (e)

Fig. 11: Spatio-temporal cross-correlations of the vertical component of the velocity field filtered for the mode 1 resonance (620 Hz). Reference velocity at *x*=101.6 mm, *y*=-10 mm; Mach 0.8.

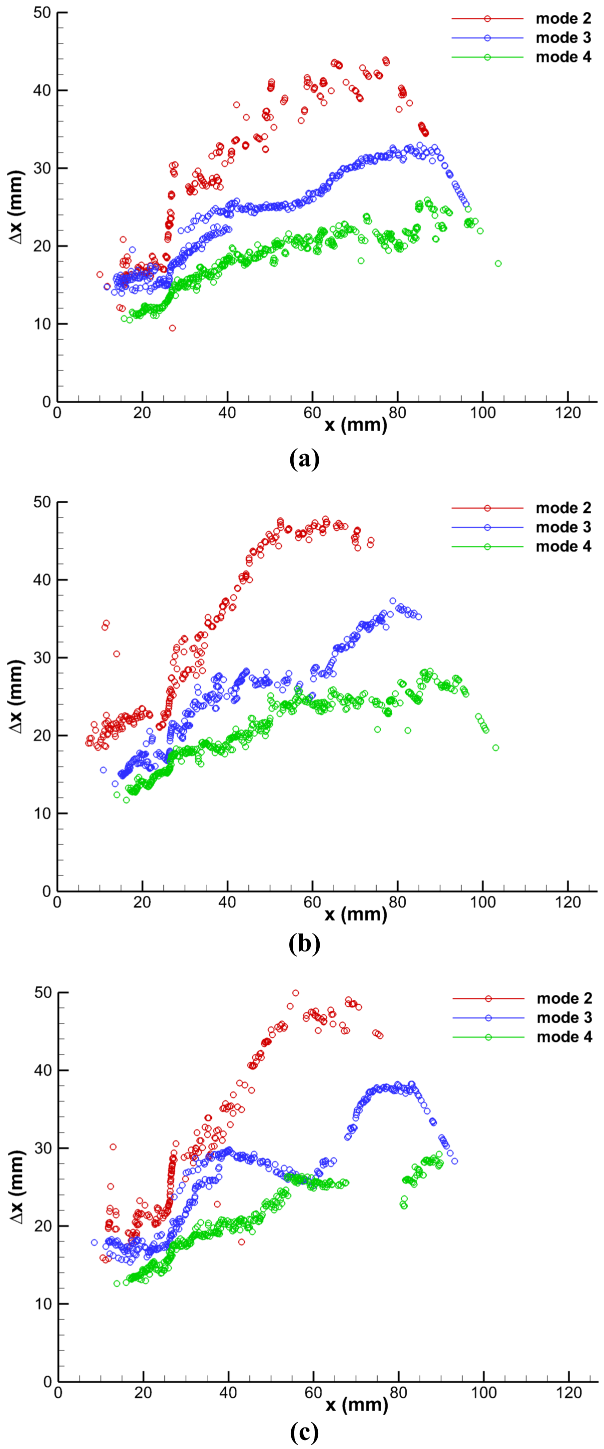

(a)

(b)

(c)

Fig. 12: Streamwise spacing of coherent structures determined from cross-correlations of filtered velocity fields. (a) Mach 0.6; (b) Mach 0.8; (c) Mach 0.94.

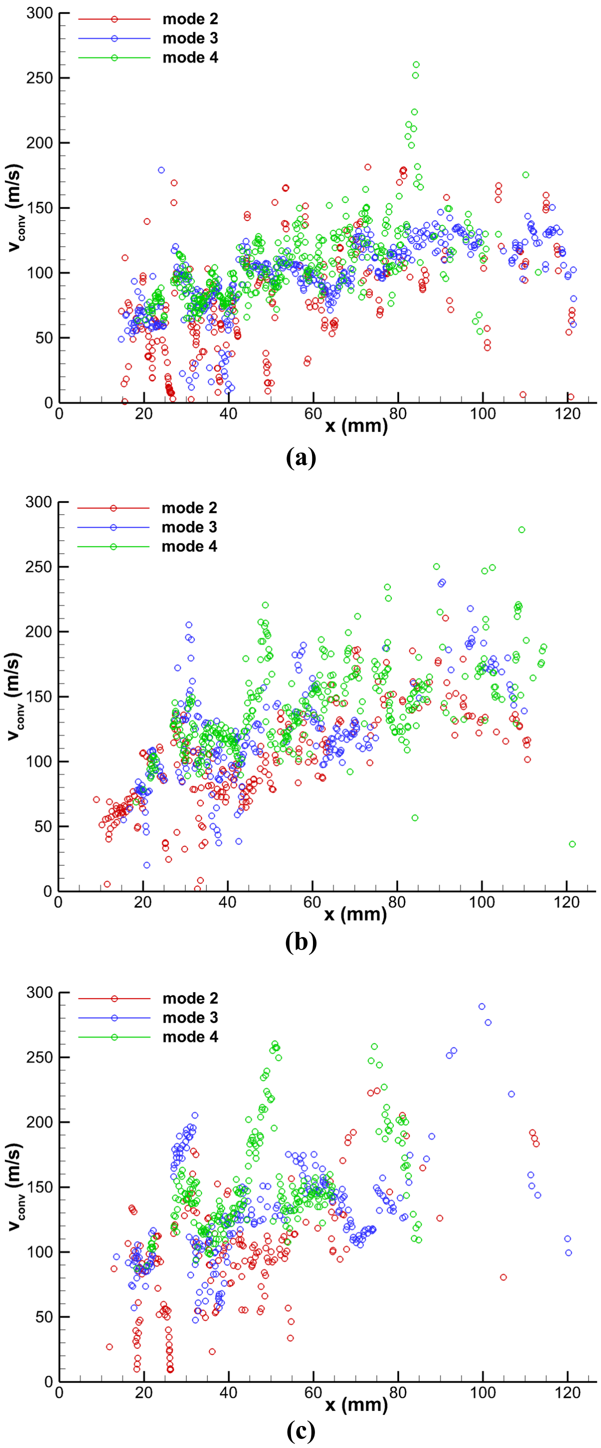

(a)

(b)

(c)

Fig. 13: Convection velocities of coherent structures determined from cross-correlations of filtered velocity fields. (a) Mach 0.6; (b) Mach 0.8; (c) Mach 0.94.

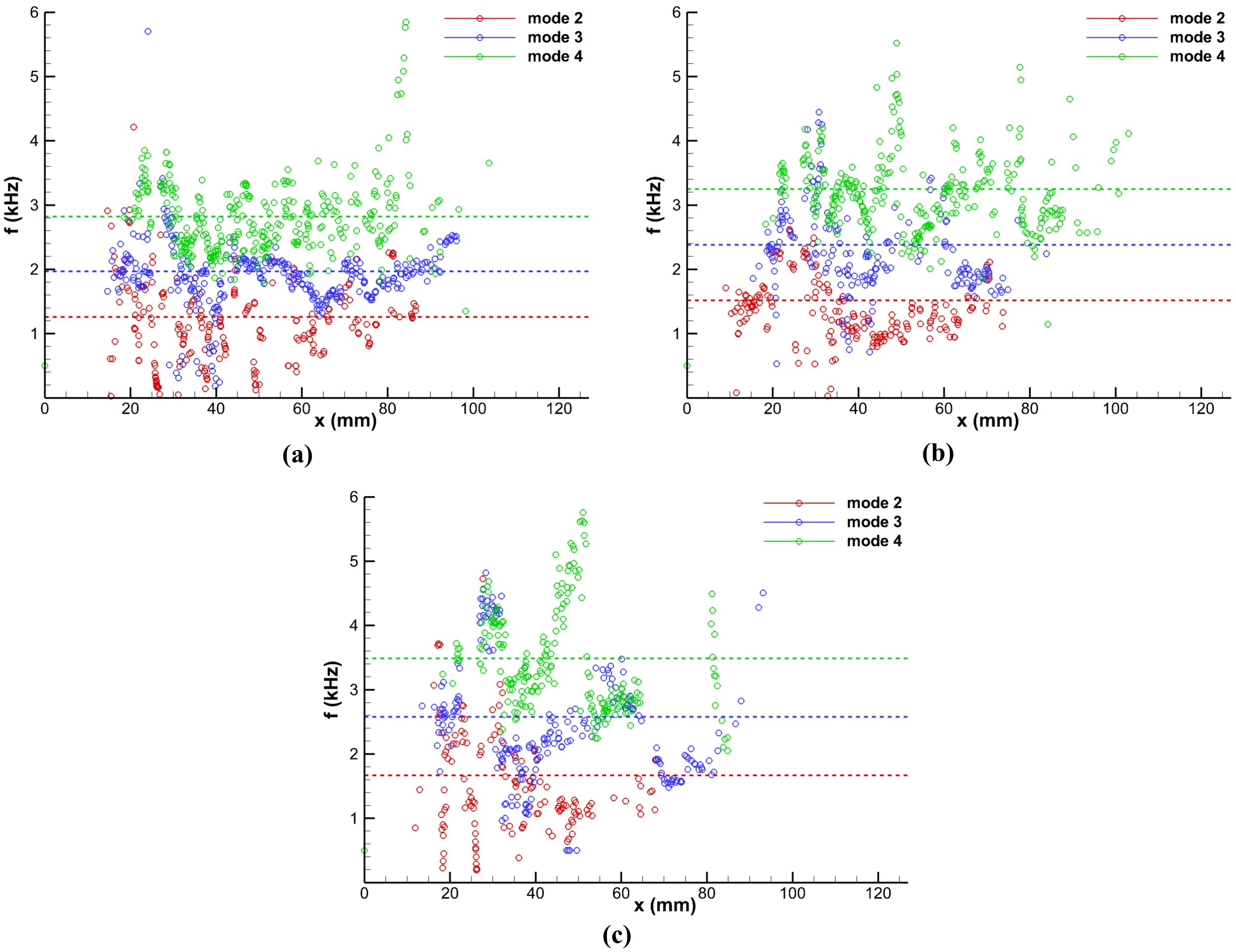

(a)

(b)

(c)

Fig. 14: Characteristic frequencies of coherent structures determined from spacing and convection velocity estimates using cross-correlations of filtered velocity fields. Dashed lines denote the resonance frequencies measured using wall pressure sensors. (a) Mach 0.6; (b) Mach 0.8; (c) Mach 0.94.